Ultra-High-Temperature Testing of Sintered ZrB_2-based Ceramic Composites in Atmospheric Re-entry Environment

Stefano Mungiguerra[a]*, Giuseppe D. Di Martino[a], Anselmo Cecere[a], Raffaele Savino[a], Luca Zoli[b], Laura Silvestroni[b], Diletta Sciti[b]

[a] *University of Naples "Federico II", Department of Industrial Engineering, P.le Vincenzo Tecchio 80, 80125 Napoli, Italy*

[b] *National Research Council, Institute of Science and Technology for Ceramics, Via Granarolo 64, 48018 Faenza, Italy*

* Corresponding Author, e-mail: stefano.mungiguerra@unina.it

Abstract

An experimental campaign has been carried out to characterize a new class of Ultra-High-Temperature Ceramic Matrix Composites for near-zero ablation Thermal Protection Systems. Small sized specimens, with ZrB_2-based matrix and different carbon fiber architectures, were exposed to a simulated air supersonic flow generated by an arc-jet wind tunnel, achieving specific total enthalpies up to 20 MJ/kg and cold wall fully catalytic heat fluxes over 5 MW/m^2, in an aero-thermo-chemical environment representative of atmospheric re-entry. Ablation rates were estimated by means of mass and thickness measurements before and after testing, demonstrating an excellent performance of the developed materials. Surface temperatures were monitored by means of infrared pyrometers and a thermo-camera, and during all the tests a spontaneous temperature jump was observed, with temperatures that reached values over 2800 K at the steady state. Post-test microstructural analyses revealed the formation of a porous oxide layer with a thickness of few hundred microns, mainly consisting of zirconia, with substantial removal of both SiC and carbon fibers. Below the oxide, the bulk material was unaffected. Computational Fluid Dynamics simulations allowed rebuilding the thermo-fluid-dynamic and chemical flow field. Moreover, it was possible to propose an innovative correlation of the temperature jump with an increased catalytic activity and a dramatic reduction of the thermal conductivity of the oxide layers forming on the exposed part of the sample, which anyway had a key role in preserving the unoxidized bulk materials at reasonable temperatures.

Keywords: Ultra-High-Temperature Ceramic Matrix Composites; Arc-jet wind tunnel testing; Near-zero ablation; Computational Fluid Dynamic simulation; Temperature Jump

1. Introduction

New-generation hypersonic and reusable re-entry vehicles set increasingly demanding requirements for the development of high-performance Thermal Protection Systems (TPS), due to the challenges of extremely harsh aero-thermo-dynamic conditions characteristic of atmospheric re-entry, including hypersonic Mach numbers, temperatures above 2000°C, the activation of gas dissociation/recombination reactions at extremely low oxygen partial pressures, which can substantially enhance the heat flux on the exposed surface of the spacecraft [1, 2].

Over the last decades, research identified Ultra-High-Temperature Ceramic (UHTC) materials, based on transition metals carbides and diborides, as potentially promising candidates for these applications, especially in light of their high melting temperatures, strength and ablation resistance at temperatures over 2000°C [3, 4, 5]. Nevertheless, some issues related to poor oxidative behavior and mechanical properties (damage tolerance, fracture toughness, thermal shock resistance) of single and multi-phase UHTCs at high temperatures limit the applicability of these materials. The introduction of SiC or other silicon based ceramics as minority phase, in the form of particles, short/long fibers or whiskers [6, 7, 8, 9, 10], in the main refractory ceramic has been often proposed to improve damage tolerance and oxidation resistance at intermediate temperature, essentially thanks to the formation of a low-viscosity borosilicate glass protective scale [11, 12, 13]. The most recent frontiers in a research oriented to high Technology Readiness Level (TRL) applications of the UHTC technology to aerospace involve the enhancement of mechanical properties by introducing short and continuous Carbon Fiber reinforcements in a UHTC matrix, leading to the definition of the Ultra-High-Temperature Ceramic Matrix Composites (UHTCMCs) [14, 15]. Recently, flexural strength values as high as 450 MPa and 200-300 MPa were collected at 1500°C and 2100°C, respectively, demonstrating the excellent performance of UHTCMCs based on Carbon fibers preforms and HfC, ZrC, TaC and ZrB_2 matrices [16, 17, 18]. All the high temperature values were always higher than the room temperature values. Moreover, UHTCMCs based on carbon preforms and ZrB_2 matrix displayed also excellent thermal shock resistance [18], with 85% of the pristine flexural strength retained after water quenching from 1500°C to room temperature.

The overall objective is developing large ultra-refractory aerospace transportation systems components with outstanding ablation resistance and enhanced mechanical properties and reliability [19, 20, 21, 22]. To achieve this goal, testing in a relevant environment is required to properly characterize the ceramic materials in conditions representative of the real flight applications. For atmospheric re-entry TPS, the most suitable facilities are supersonic and hypersonic arc-jet wind tunnels [23, 24].

Within this framework, University of Naples "Federico II" (UNINA) and the Institute of Science and Technology for Ceramics of the Italian National Research Council (CNR-ISTEC) are involved in the Horizon 2020 European C^{3}HARME research project, focused on the development of a new class of UHTCMCs for near-zero ablation thermal protection systems [25]. An extensive experimental characterization campaign has been carried out on in the UNINA

arc-jet wind tunnel, where atmospheric re-entry conditions are reproduced at maximum flow total enthalpies higher than 20 MJ/kg, supersonic Mach number and temperatures over 2000°C in a gas atmosphere with high concentration of atomic oxygen. Non-intrusive diagnostic equipment, including two-color pyrometers and an infrared thermo-camera, is employed to monitor the surface temperature of the samples. The ablation rates of the samples after the exposure to the aero-thermo-chemically aggressive flow are also estimated by mass and thickness measurements.

We previously published the results of an arc-jet wind tunnel characterization campaign carried out on a batch of two UHTCMC samples with ZrB_2-10 vol% SiC as matrix and ~50 vol% of continuous coated PAN-based carbon fibers as reinforcing phase [26]. The present work extends the results to 3 more samples, all based on a UHTC matrix with ZrB_2 as major component and SiC and Y_2O_3 particles as minority phase, reinforced with uncoated continuous or chopped ultra-high modulus pitch-based carbon fibers. Compared to the previous work [26], in this one, we notably improved the manufacturing of UHTCMCs. The matrix was nearly pore–free, the matrix phase distribution in the fiber preform was more homogenous. These two features are of fundamental importance to guarantee a better protection of the fibers by the UHTC matrix during oxidation and hence arc-jet tests, as explained in [15].

The outcomes of the experimental activities are presented and discussed, also in light of the post-test characterizations carried out to investigate the features of the materials microstructures after the exposure to the atmospheric re-entry environment. Moreover, the experimental results are complemented by Computational Fluid Dynamics (CFD) simulations, employed to allow accurate prediction not only of the thermo-fluid-dynamic flow field around the test articles, but also of the thermal behavior of the materials samples, including an investigation of the effect of material properties, such as thermal conductivity and catalycity.

Specifically, a rapid temperature increment during the highest-enthalpy steps, phenomenon known as “temperature jump” in the relevant literature regarding UHTCs and SiC-based ceramics, has been observed [27, 28, 29]. This paper intends to propose a thorough and detailed analysis of the materials aero-thermo-dynamic behavior at ultra-high temperatures in a representative re-entry environment, aiming to provide a comprehensive interpretation of the temperature jump, correlating the outcomes of infrared temperature measurements, post-test microstructural analyses and numerical simulations to highlight the parameters which mainly affect the heat transfer from the flow to the ceramic. A deep understanding of the materials response is indeed an important step in the path towards a reliable engineering application of these novel TPS technologies.

2. Materials and methods

2.1. Material processing

Different matrix formulations and carbon fibers architectures have been compared. UHTC matrices containing different amount and type of additives (SiC and Y_2O_3) were prepared by conventional wet powder milling technique, Table 1. SiC is a common secondary phase added into UHTC matrices to increase the oxidation resistance and mechanical properties, Y_2O_3 is introduced with the aim of improving the oxide stability, i.e. preventing the ZrO_2 martensitic transformation and corresponding volume expansion upon cooling. Regarding fiber, both random chopped fibers and continuous fibers alternately arranged with 0° and 90° orientation have been considered.

Sample ID	UHTC, vol%	FVC, vol%	Fiber type
ZS5Y-SF	ZrB_2 + 5SiC + 5 Y_2O_3	40	short, XN60
ZS10Y-SF	ZrB_2 + 10SiC + 5 Y_2O_3	45	short, XN60
ZS10Y-LF	ZrB_2 + 10SiC + 5 Y_2O_3	35	long, XN80

Table 1. List of matrix compositions and fiber volume fraction (FVC) of the investigated UHTCMCs.

Short fibers were added to the UHTC powders and mixed for 24 hours. The slurries were then dried in a rotary evaporator and de-agglomerated. Long fiber-reinforced materials were obtained by aqueous slurry infiltration, stacking of the Cf foils with a 0°/90° configuration and drying in air.

Composites were densified to full density after sintering at 1900°C as described in [30, 19]. Typical images of the microstructures taken by scanning electron microscopy (FE-SEM, Carl Zeiss Sigma NTS Gmbh, Oberkochen, DE) are displayed in Fig. 1. All composites had large defect-free microstructure. Short-fiber, with length around 150 μm, were homogeneously dispersed into the ZrB_2-based matrix with preferential orientation along the xy axis, Fig. 1(a). Long-fiber reinforced materials presented some perpendicular micro-cracks between the fabric layers, but good fiber infiltration and 0° to 90° layers adhesion was achieved.

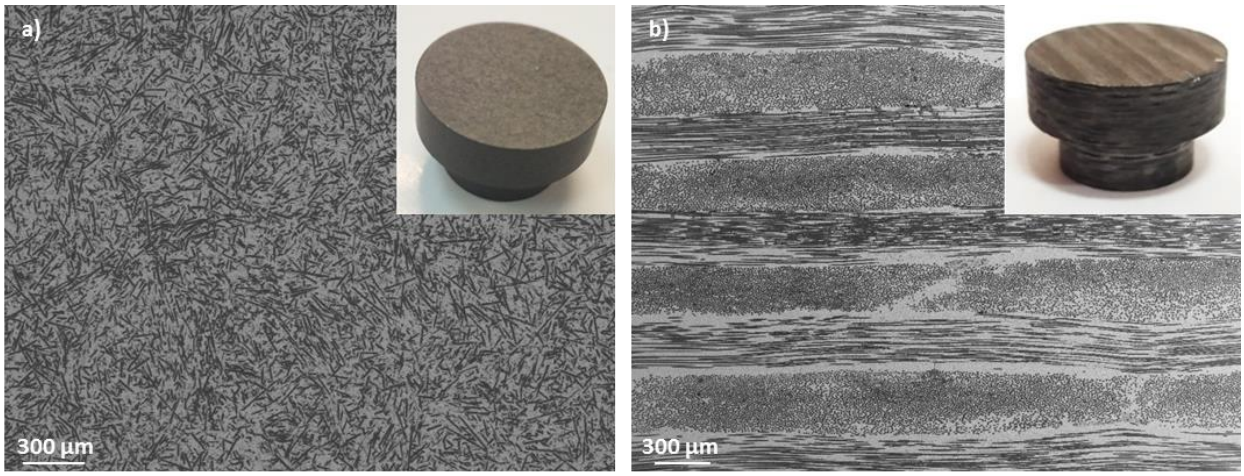

Fig. 1. Sample pictures (top right frame) and typical microstructure of as-sintered UHTC reinforced with a) short fiber or b) long fiber with 0°/90° architecture.

2.2. Arc-jet facility

Experimental tests were carried out in the arc-jet wind tunnel available at the University of Naples "Federico II", named SPES (Small Planetary Entry Simulator). This is an open circuit, continuous wind tunnel where a nitrogen plasma can be generated by an industrial torch able to operate at powers up to 80 kW and mixed to a secondary cold oxygen flow in order to simulate earth atmospheric composition. A converging-diverging nozzle is employed to expand the hot mixture to a nominal supersonic Mach number equal to 3. A detailed facility description can be found in [31].

Small sized material samples can be placed downstream the nozzle exit section by a dedicated thermally protected supporting mechanism, in order to expose them to the supersonic dissociated air flow, and characterize materials response to the extreme aero-thermo-chemical environment [32]. The nominal samples design for the present test campaign is that typically used in the arc-jet facility [28] and is displayed in Fig. 2. The UHTCMC samples were placed at a distance of 1 cm from nozzle exit.

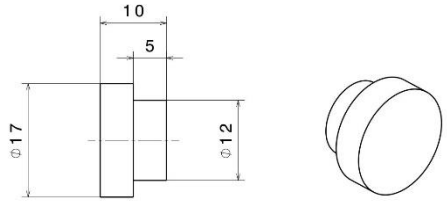

Fig. 2. Nominal design of UHTCMC samples. Dimensions in mm.

In the present test campaign, samples were exposed to a supersonic flow generated by the expansion of a high enthalpy gas mixture of nitrogen (0.8 g/s) and oxygen (0.2 g/s). During the test, the arc power of the plasma torch and consequently the total enthalpy of the flow were gradually increased through successive increments, leading correspondingly to an increase of pressure and temperature. A quasi-stationary condition generally occurs when the maximum value of temperature is reached during the last steps of the test. In the tests discussed in the present work, the nominal duration of each step was 30 seconds, except for the last step of 120 seconds. The specific total enthalpy is obtained, with an uncertainty around 10%, through an energy balance at the exit of the plasma torch, based on measurement of temperature and flow rate of cooling water [31]. The values of specific total enthalpy corresponding to each power step are reported in Table 2. After reaching the maximum enthalpy level, the arc power is gradually decreased until facility shutdown.

Table 2. Specific total enthalpies at different steps during the tests.

Step	1	2	3	4	5	6	7	8
H_0 [MJ/kg]	7.0	8.5	10	12	14	16	18	20

The surface temperature of the samples was continuously measured (±1% instrumental accuracy) by digital two-color pyrometers (Infratherm ISQ5 and IGAR6, Impac Electronic GmbH, Germany) at an acquisition rate of 100 Hz. In addition, an infrared (IR) thermo-camera (TC, Pyroview 512N, DIAS Infrared GmbH, Germany) allows for the evaluation of the temperature distribution over the sample surface. The ISQ5 pyrometer exploits two overlapping infrared wavelength bands at 0.7–1.15 µm and 0.97–1.15 µm to measure the actual temperature from 1273 K up to 3273 K. The IGAR6 pyrometer operates in the bands 1.5-1.6 µm and 2.0-2.5 µm to return the sample temperature in the range 523-2273 K. The measurement area of the ISQ5 pyrometer is approximately a round spot 3.3 mm in diameter.

The thermo-camera is able to detect temperature in the range 873-3273 K and it operates in the spectral range from 0.8 to 1.1 μm. The temperature measurement of the IR-TC is dependent on the surface emissivity ε_λ in the instrument operating spectral range. In order to set the correct value of the spectral emittance, the TC measurement is compared to the actual temperature detected by the pyrometers in the two-color mode, and the value of ε_λ is adjusted until the TC gives back the same temperature as the pyrometers. High-Definition videos of the tests were recorded by means of a Camera Flea3 1.3 MP Color USB3 Vision with a resolution of 1328x1048 and a frame rate equal to 25 fps.

A balance (1 mg accuracy) and a precision caliper (0.01 mm accuracy) were used to measure mass and thickness losses of the specimen. In the post-processing analyses, two erosion rates were calculated: one based on the loss of mass (assuming uniform consumption of the sample in the axial direction) and the other evaluated by the thickness measurement made by the caliper.

2.3. Numerical models

In order to properly characterize the flow field inside the facility and to rebuild the thermal behavior of the samples, Computational Fluid Dynamics (CFD) simulations were performed. In particular, steady-state simulations of the flow field are performed, solving the Reynolds-Averaged Navier-Stokes equations for a turbulent multi-reacting gas mixture with five species (i.e. O, O_2, NO, N and N_2), in chemical non-equilibrium, considering finite rate chemical reactions, with the reaction rate constants specified by the Arrhenius law [33].

The flow simulations were performed in two steps. First the 2D-axisymmetric computational domain shown in Fig. 3(a) was considered, including the mixing chamber, where N_2 coming from the torch and cold O_2 are mixed, and the converging-diverging nozzle, where the high-enthalpy simulated air flow is expanded to supersonic conditions. The total temperature and chemical composition of the gas coming from the torch, at nitrogen inlet, were evaluated by means of the NASA CEA (Chemical Equilibrium with Applications) software [34] in order to match the total specific enthalpy corresponding to the desired value of the torch arc power. A radial mass flow inlet provides cold oxygen injection. Nozzle water-cooling was taken into account by setting a temperature boundary condition on the nozzle walls (T = 400 K). The main output of these simulations were the thermo-fluid-dynamic and chemical conditions achieved at nozzle exit section, which was modelled as a supersonic pressure outlet and corresponds to the inlet of the test chamber.

In the second simulation step, the aero-thermo-dynamic flow field around the sample and its supporting system was calculated, using the computational grid shown in Fig. 3(b). The main quantities of interest (temperature, pressure, velocity and chemical composition) calculated at the nozzle exit section in the previous step, were assigned to a boundary representing the inlet of the flow into the test chamber (bottom left of Fig. 3(b)). On the top and rear boundaries of the test chamber domain, a pressure-outlet condition corresponding to the experimental vacuum environment was set.

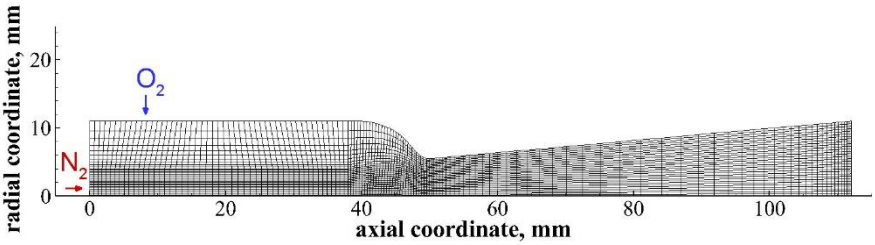

(a)

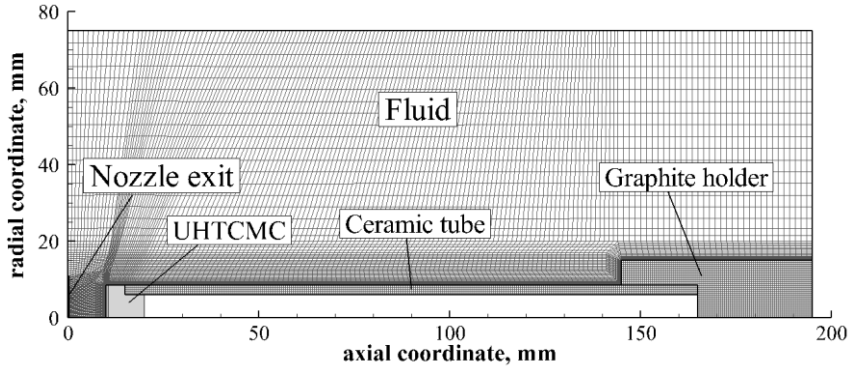

(b)

Fig. 3. Mesh for the CFD simulations: a) mixing chamber and nozzle; b) test chamber, including test sample and solid supporting system.

The surfaces of the solid components were first treated as cold walls (T = 300 K), for the calculation of the convective heat flux. Subsequently, the thermal behavior of the UHTCMC sample was simulated by solving the energy

equation inside the solid components, considering thermal coupling between fluid and solid domain, by means of temperature and heat flux continuities at the interfaces.

Due to the high concentration of dissociated species in the flow, particular focus was given to the effect of surface catalycity, which enhances the heat transfer to the sample. The non-catalytic (NC) condition was specified by assigning, for each species, a zero diffusive flux in the direction normal to the specimen surface. The fully catalytic condition (FC) was set by assigning, on the sample surface, the species mass fractions corresponding to a complete recombination of atoms into molecules. Intermediate values of the catalytic recombination coefficients γ_w [35, 36] can also be considered, according to the model described in [26]. In this paper, to reduce the number of unknown quantities, it has been assumed that the catalytic recombination coefficients are the same for the two atomic species, nitrogen and oxygen.

A more detailed description of the numerical models employed in this work can be found in [26, 37].

3. Experimental results

3.1. Arc-jet testing

Table 3 summarizes the test conditions to which each sample was subjected, in terms of the enthalpy steps described in Table 2. The thermal histories of the different samples, measured by the ISQ5 pyrometer, are plotted in Fig. 4.

Table 3. Test conditions achieved for each sample.

Sample ID	Enthalpy steps	T max achieved, K
ZS5Y-SF	2-7	2690
ZS10Y-SF	1-8	2850
ZS10Y-LF	2-7	2700

The stepwise increase in temperature is associated to the power increase procedure. At the maximum enthalpy level, the temperatures of all the samples reached values close to 2700 K and even overpassed 2800 K for the only sample tested at the highest power condition, ZS10Y-SF. In particular, it was clear that a sudden rise in temperature (herein defined as "temperature jump") of several hundred degrees occurred during the highest-enthalpy steps, even at a constant arc power, after a steady state condition had apparently been reached. The jump happened for all the samples when the flow specific total enthalpy was 18 MJ/kg. For sample ZS5Y-SF the jump occurred around t = 150 s, few seconds after the surface temperature reached a stable value over 2250 K, while for samples ZS10Y-SF and ZS10Y-LF, the momentary equilibrium temperature was around 2150 K (achieved a t = 160 s and 180 s, respectively). For sample ZS10Y-SF the torch arc power was further increased to the maximum value (H_0 = 20 MJ/kg) at t = 180 s, when the jump had already been triggered and the surface temperature was 2270 K, resulting in an increased slope of the temperature time profile and a surface temperature exceeding 2800 K at the end of the heating phase. The temperature jump phenomenon is typically observed for UHTC- and SiC-based composites [27, 28, 29] and can be associated to a drastic change in surface chemistry, as will be widely discussed later on.

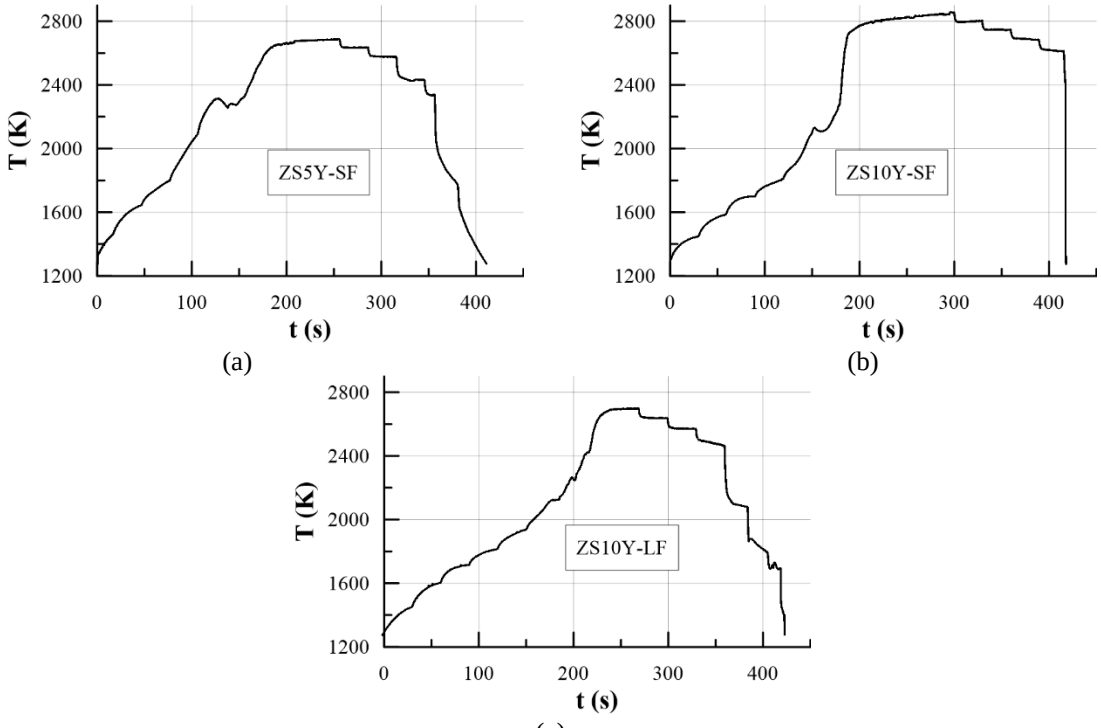

Fig. 4. Temperature histories of the samples, measured by the ISQ5 pyrometer.

After the tests, all samples heads appeared completely oxidized, with a white layer, mainly composed of ZrO_2, as discussed below, covering the surface. For samples described earlier [26], this layer had been found to be porous, fragile and with tendency to spall off. In the present test campaign, the samples preserved instead the original shape and a perfect structural integrity, despite the clearly noticeable signs of surface oxidation (see Fig. 5). The long-fiber layered architecture of samples ZS10Y-LF was still observable (see Fig. 5(c)).

The average mass- and thickness-based erosion rates are reported in Table 4 and all of them are on the order of 10^{-4} mm/s. Balance between oxygen inclusion and C, Si and B volatilization upon sample oxidation resulted in a net, although limited, mass loss. It is interesting to observe that, on the other hand, oxidation led to a thickening of samples heads, resulting in a negative ablation rate based on thickness measurement. Since no other samples dimensions had significant variations with respect to the nominal values (Fig. 2), only thickness data are here reported. Based on these measurements, it can be concluded that all the samples experienced a slight volume increase despite the net mass loss.

(a) (b) (c)

Fig. 5. Pictures of samples after test: a) ZS5Y-SF, b) ZS10Y-SF, c) ZS10Y-LF.

Table 4. Mass and thickness data before and after the test.

	ZS5Y-SF	ZS10Y-SF	ZS10Y-LF
Initial mass	7.360 g	6.709 g	7.374 g
Final mass	7.270 g	6.553 g	7.300 g
Average erosion rate (mass)	$3.0 \cdot 10^{-4}$ mm/s	$5.6 \cdot 10^{-4}$ mm/s	$2.5 \cdot 10^{-4}$ mm/s
Initial thickness	4.90 mm	5.01 mm	4.98 mm
Final thickness	5.00 mm	5.05 mm	5.01 mm
Average erosion rate (thickness)	$-3.2 \cdot 10^{-4}$ mm/s	$-1.3 \cdot 10^{-4}$ mm/s	$-1.0 \cdot 10^{-4}$ mm/s

The IR video of test on sample ZS5Y-SF showed that, few seconds before the temperature jump, an unsteady evolution of the irradiated power appeared on the side surface, resulting in a wavy oscillation of the surface temperature. A comparable phenomenon has been already reported by Monteverde et al. [31], who defined it as *waves-of-radiance* and correlated it to the transport of a liquid glassy oxide phase from the front surface along the side of the sample by the shear stresses induced by the supersonic flow. A qualitative visualization of the phenomenon is possible, watching the IR video provided in the Supplementary material. Evidence of the *waves-of-radiance* can be observed also in Fig. 6 and Fig. 7, which are referred, as examples, to samples ZS5Y-SF and ZS10Y-LF, respectively. The diagrams on the left (Fig. 6(a) and 7(a)) show the temperature axial profiles measured by the TC on the side surface of the samples, each curve representing a specific time instant at the earliest stages of the temperature jump. The diagrams on the right (Fig. 6(b) and 7(b)) report instead the time evolution of the temperature at different locations along the surface. The curves have been obtained assuming a constant spectral emissivity along the whole surface, so they should be more correctly interpreted as surface radiance profiles, rather than actual temperature diagrams. Two features can be remarked. First, the axial profiles of Figs. 6 and 7(a) are not straight, but temperature oscillations can be noticed, up to around 20 K. The same behavior was observed in [31]. Moreover, it is possible to see that, as time advances, the radiation temperature does not change uniformly along the samples length, but the distance between two curves corresponding to consecutive instants is variable, and in some case the lines even cross each other. This phenomenon is evidenced also in the pictures on the right (Figs. 6 and 7(b)). The curves display an oscillatory trend and tend to get closer and farther as time advances, testifying an unsteady evolution of the radiated power which is different at each axial location.

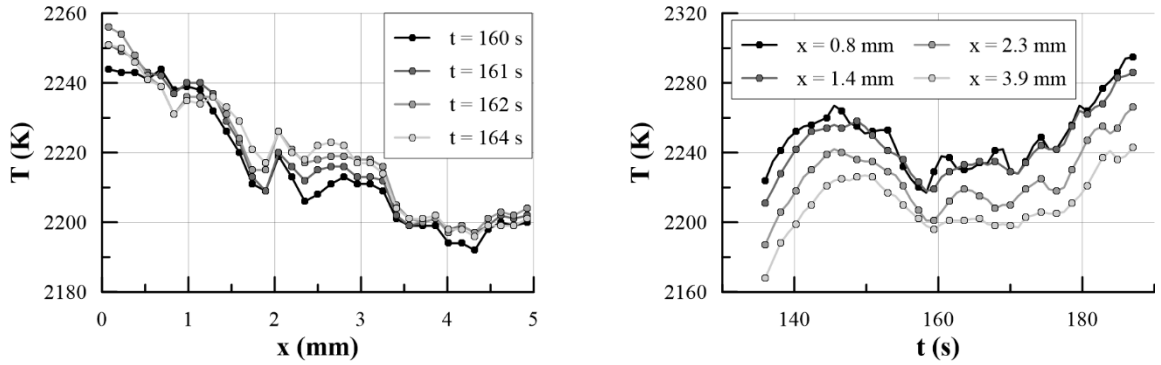

(a) (b)

Fig. 6. ZS5Y-SF: a) Temperature axial profiles, measured by IR-TC before temperature jump; b) Time evolution of the IR-measured temperature at different points along the sample side surface.

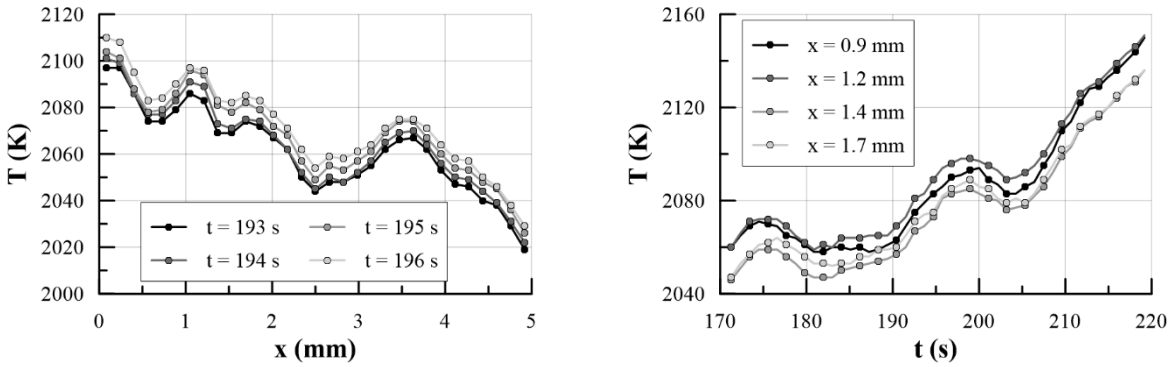

(a) (b)

Fig. 7. ZS10Y-LF: a) Temperature axial profiles, measured by IR-TC before temperature jump; b) Time evolution of the IR-measured temperature at different points along the sample side surface.

For a sound analysis of the material thermal behavior during arc-jet testing, infrared measurements on sample ZS10Y-LF were taken as reference. During the tests, the ISQ5 pyrometer was pointed towards the sample front face, whereas the IGAR6 pyrometer looked at the side surface. Moreover, the IR thermo-camera positioning allowed to analyze both the front and the side surfaces facilitating the visualization and characterization of the temperature jump phenomenon. Fig. 8(a) and (b) show the thermal distribution on the sample respectively just before and just after the jump, during the maximum enthalpy step (H_0 = 18 MJ/kg). It is evident that only the front part of the sample experienced a dramatic increase in temperature, whereas the rear body appeared to be almost unaffected by the thermal rise. The same trend is visible in Fig. 9, where the thermal histories recorded by the two pyrometers for the two surfaces of the sample are shown. It is evident that the measurements matched well in the earliest phases of the test, whereas, at temperatures over 2100 K, they started diverging, and the front face reached a steady-state temperature around 500 K higher than the side.

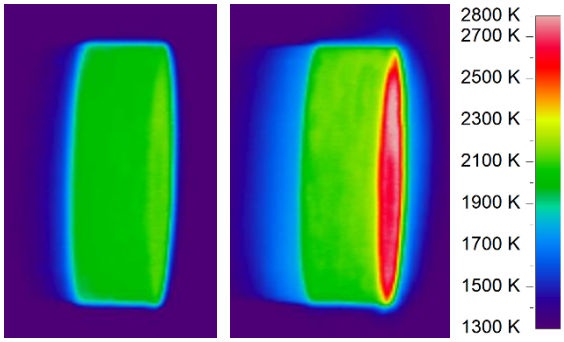

(a) (b)

Fig. 8. Thermal images of sample ZS10Y-LF (a) before and (b) after the temperature jump.

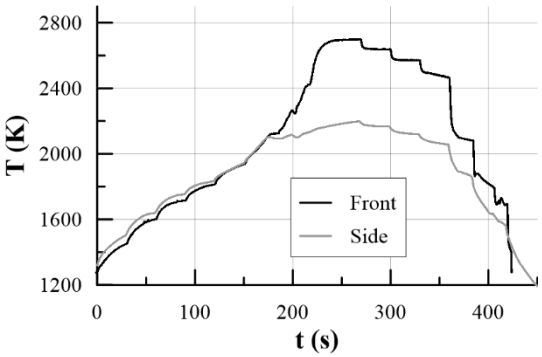

Fig. 9 Comparison of temperature measured by ISQ5 pyrometer (front surface) and IGAR6 pyrometer (side surface) for sample ZS10Y-LF.

Thermo-camera and pyrometers measurements were compared to provide an estimation of the spectral emissivity in the near infrared wavelength band, which is common to all instruments. Fig. 10 shows the temperature curves collected by pyrometers and thermo-camera, on front (a) and on side (b) surfaces of sample ZS10Y-LF, assuming a spectral emissivity $\varepsilon_\lambda = 0.7$. The non-perfect overlapping suggests a change in emissivity during heating. This trend is quantified in Fig. 11, where the value of ε_λ, evaluated by matching the pyrometer and thermo-camera measurements as described in section 2.2, is plotted versus test time for both the front (black line) and side (gray line) surfaces of sample ZS10Y-LF. Spectral emissivity appears to increase in the earliest phases of the test, from a value below 0.4 after 30 s (end of first enthalpy step) up to over 0.7, after roughly 60 s (end of second enthalpy step). Then, ε_λ gradually decreases during heating on both surfaces, attaining a minimum value between 0.5 and 0.6 and then rapidly increasing again after the temperature jump up to almost 0.8. Finally, it appears that, during the cooling phase, the emissivity rapidly decreases on the front surface, while it is almost constant on the side.

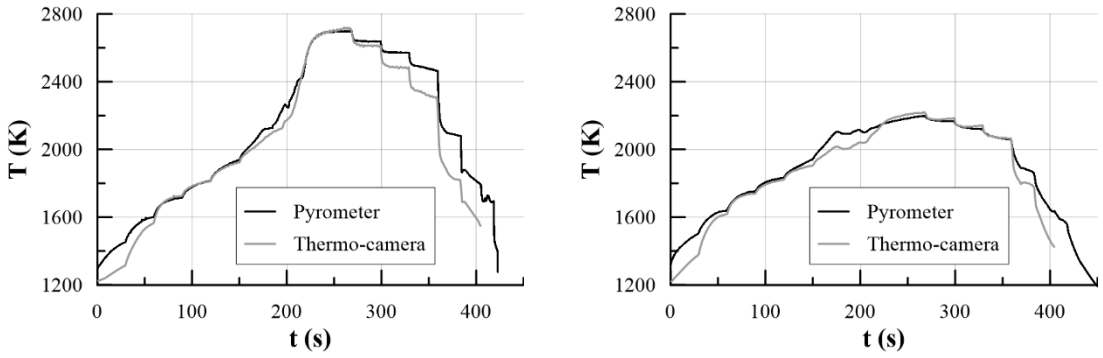

Fig. 10. Comparison between temperature measured by pyrometers and thermo-camera ($\varepsilon_\lambda = 0.7$) (a) on the front surface and (b) on the side surface, of sample ZS10Y-LF.

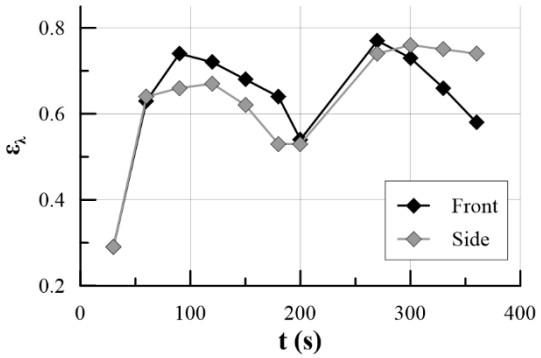

Fig. 11. Spectral emissivity in the near-infrared wavelength band on front and side surface of sample ZS10Y-LF, versus test time.

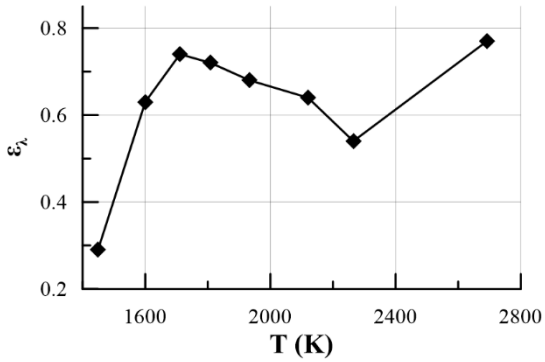

Fig. 12. Spectral emissivity in the near-infrared wavelength band for sample ZS10Y-LF, versus temperature.

3.2. Post-test microstructure analysis

In order to implement the numerical calculation and gain an insight into the samples aerothermal behavior during arc-jet testing, post-test microstructures were analyzed by SEM and energy dispersive x-ray spectroscopy (EDS, INCA Energy 300, Oxford instruments, UK).

Comparative views of the external oxidized surface of the samples with short fibers is reported in Fig. 13. It can be appreciated that in both cases, the surfaces were fiber-free, ZS5Y-SF displayed alternated areas with dense ZrO_2 or cracked and porous ZrO_2, Fig. 13(a), whereas ZS10Y-SF was featured by diffused cracking in a ZrO_2 layer with large pores which coated another one where finer pores could be seen, Fig. 13(b). This structure suggests that partial oxide removal took place leaving uncoated the oxide layer underneath. To note that XRD analysis on these surfaces confirmed that the ZrO_2 scale maintained the tetragonal structure owing to the stabilization by Y_2O_3. Therefore, cracking in ZS10Y-SF might be due to the thermal stress rising from coupling of ZrO_2 with different pore size and volume fraction.

EDS elemental analysis of the cross section in the central area of the model, Fig. 14, evidenced an oxygen depth penetration of 400 and about 550 μm in ZS5Y-SF and ZS10Y-SF, respectively, in agreement with the severity of the test conditions. Interesting to note is Si distribution across the scale: in the less harsh condition, ZS5Y-SF, Si accumulated towards the top surface and filled ZrO_2 scale in the sub-layer. In the hardest condition, ZS10Y-SF, no SiO_2-based topping accumulated owing to its instant evaporation once the outermost surface once was achieved.

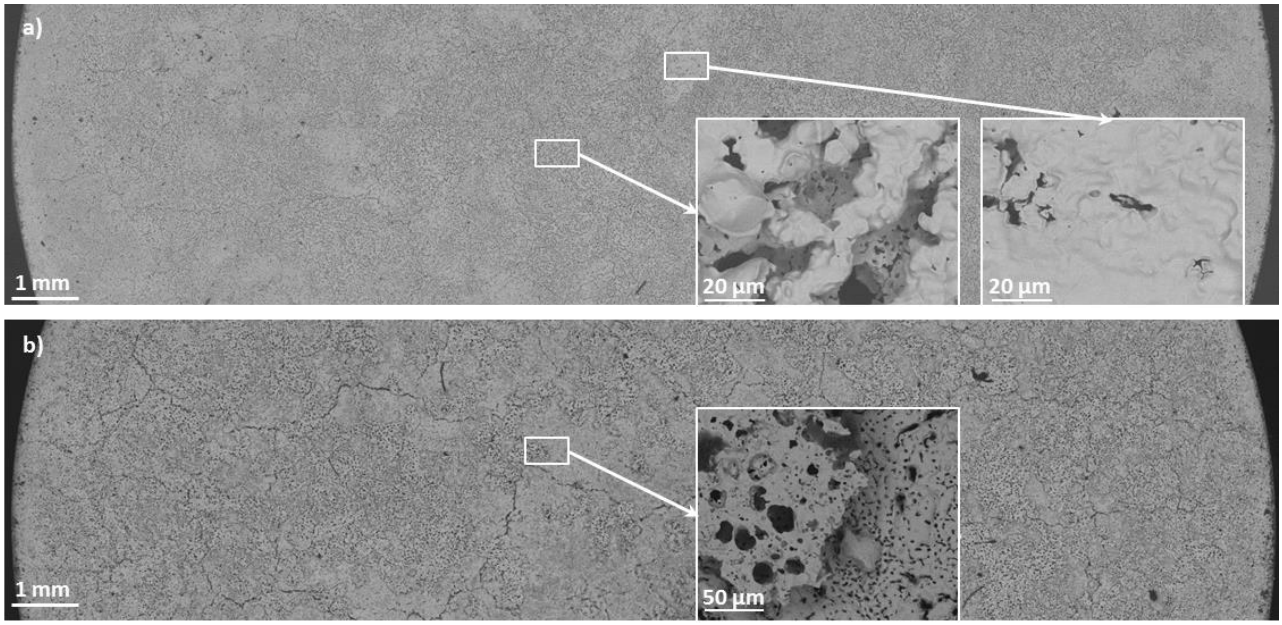

Fig. 13. SEM images of the surface of the short fiber reinforced samples after arc-jet tests with enlarged views of microstructural details inset: a) ZS5Y-SF, b) ZS10Y-SF.

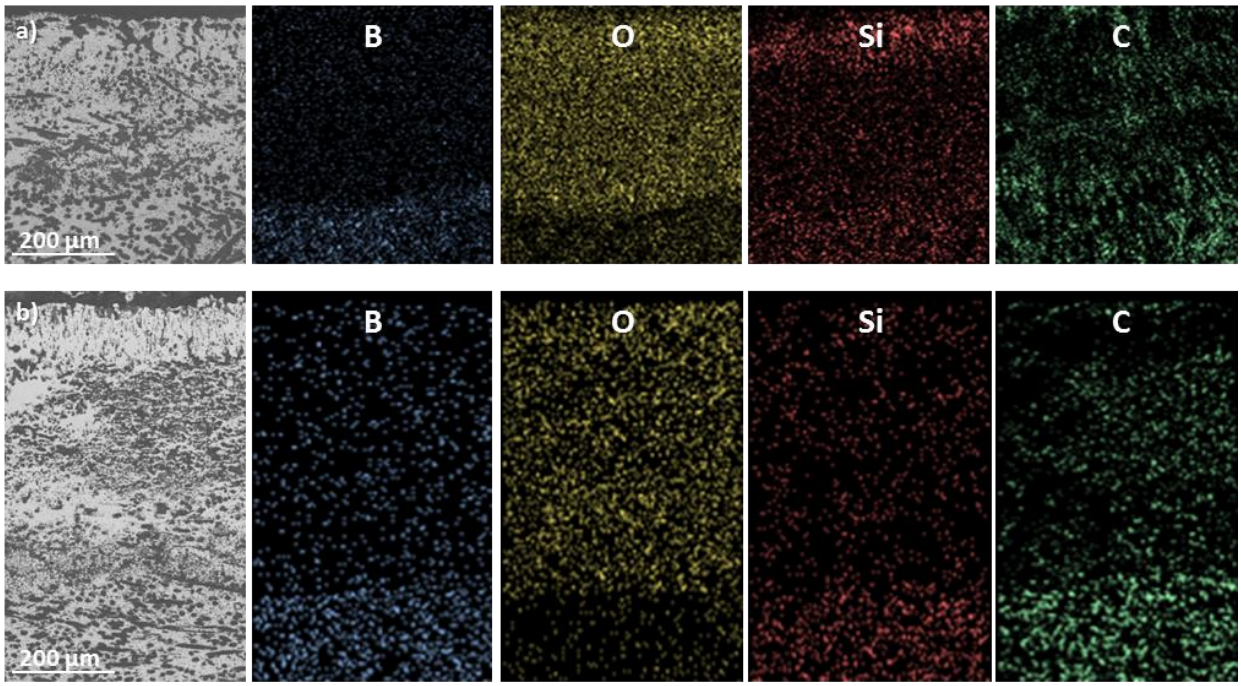

Fig. 14. SEM image and corresponding EDS elemental mapping of a) ZS5Y-SF, b) ZS10Y-SF samples taken from the central zone of the buttons.

Magnified views of the cross section of the SF samples are shown in Fig. 15. In both cases the unaffected core and oxide scale had a strong and coherent interface, carbon fibers did not survive in the ZrO_2 layer and silica-based accumulation was clear only in ZS5Y-SF, Fig. 15(a). In the case of ZS10Y-SF, despite the embrittlement of the sub-layer owing to the fiber consumption, no spalling occurred, possibly owing to a stable oxide composition which comprised ZrO_2 and a mixed Y-B-C-O phase. As for the matrix composition containing 5 or 10 vol% SiC in ZS5Y-SF and ZS10Y-SF, respectively, one could think that higher amount of SiC would provide better oxidation resistance, owing to the higher source of protective silica glass [38]. However, under these experimental conditions, SiC volume fraction seems not to play such a relevant role, because most of the glass migrated to the surface (which could retard the advancement of the oxidation front), was shear-transported away and vaporized at the ultra-high temperatures of 2700-2800 K.

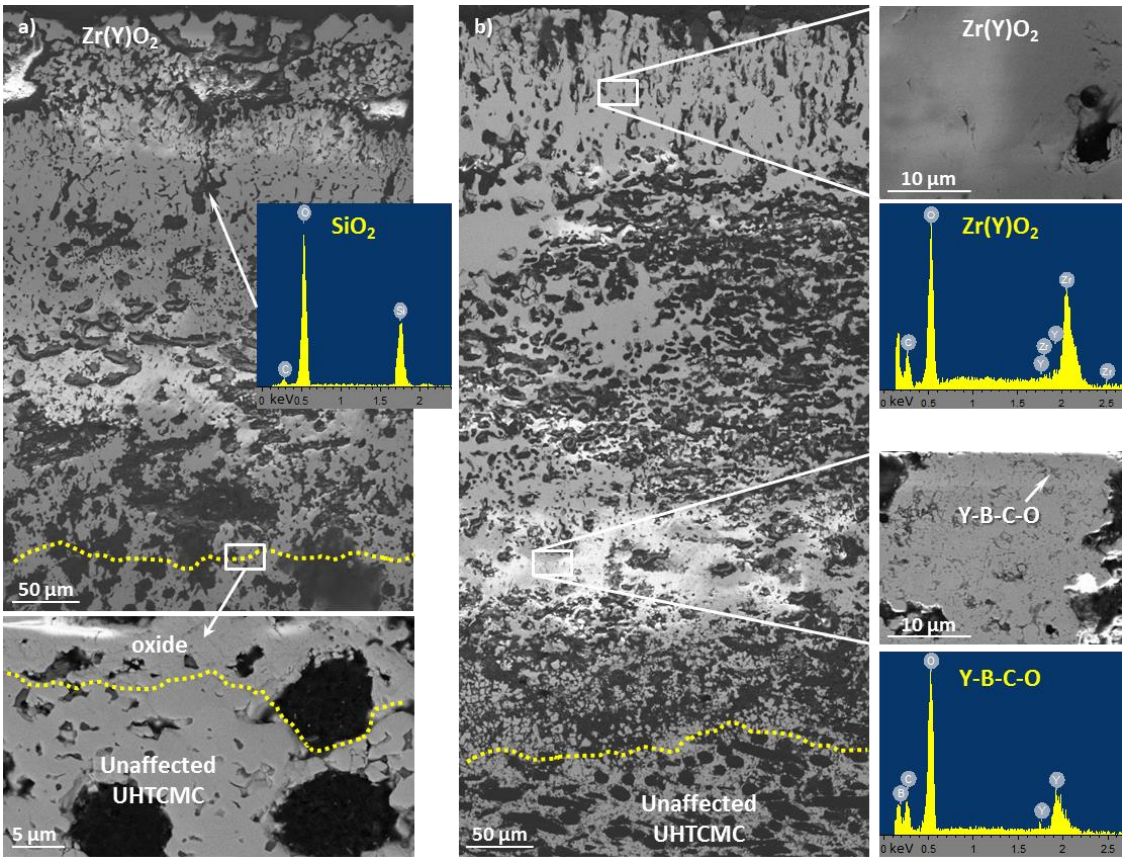

Fig. 15. SEM images of the cross sections of a) ZS5Y-SF, b) ZS10Y-SF samples showing the oxide architecture.

Moving to the long-fiber UHTCMC, the outer surface presented discontinuous zones of silica-based rich glass and a sort of ZrO_2 sheath of the carbon fiber which were ablated away, Fig. 16. Fig. 17 shows SEM pictures of the ZS10Y-LF sample cross-section after exposure to the supersonic plasma flow with EDS mapping of the main components and a zoom on the outermost oxide layer. The overall oxide layer had a thickness of around 360 µm, which approximately corresponds to the thickness of one fabric scale. The oxide appeared more damaged and brittle in the center as compared to the periphery where it was rather compact smooth. Below this layer, the pristine microstructure appeared unaffected, with evidence of the 0°/90° architecture of the fibers. EDS revealed complete boron removal in the region of oxygen penetration, whilst silicon was slightly depleted in the subscale and accumulated close to the surface. At higher magnification, the outermost layer comprised a roughly 50µm-thick pure ZrO_2 region, which displayed an irregular and highly porous structure. Below this, a silica-rich layer was present, which covered a SiC-depleted region, where voids were left by Si outwards diffusion. Also in this case, there was no evidence of carbon fibers survival to the exposure to the arc-jet flow, all along the oxide thickness.

It can be stated that the long fiber configuration was very effective in limiting oxygen penetration across the material depth, possibly thanks to the consumption of one carbon fabric sheet that locally enriched the environment in CO, thus contrasting oxygen advancement.

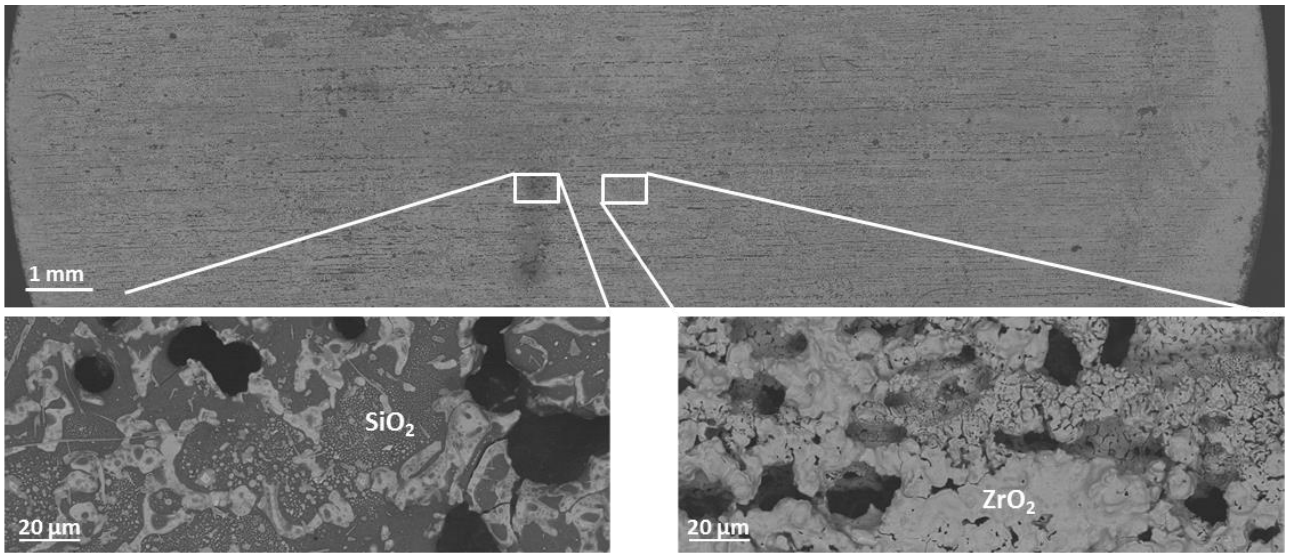

Fig. 16. SEM images of the surface of the long fiber reinforced sample after arc-jet tests, ZS10Y-LF, with enlarged views of microstructural details inset.

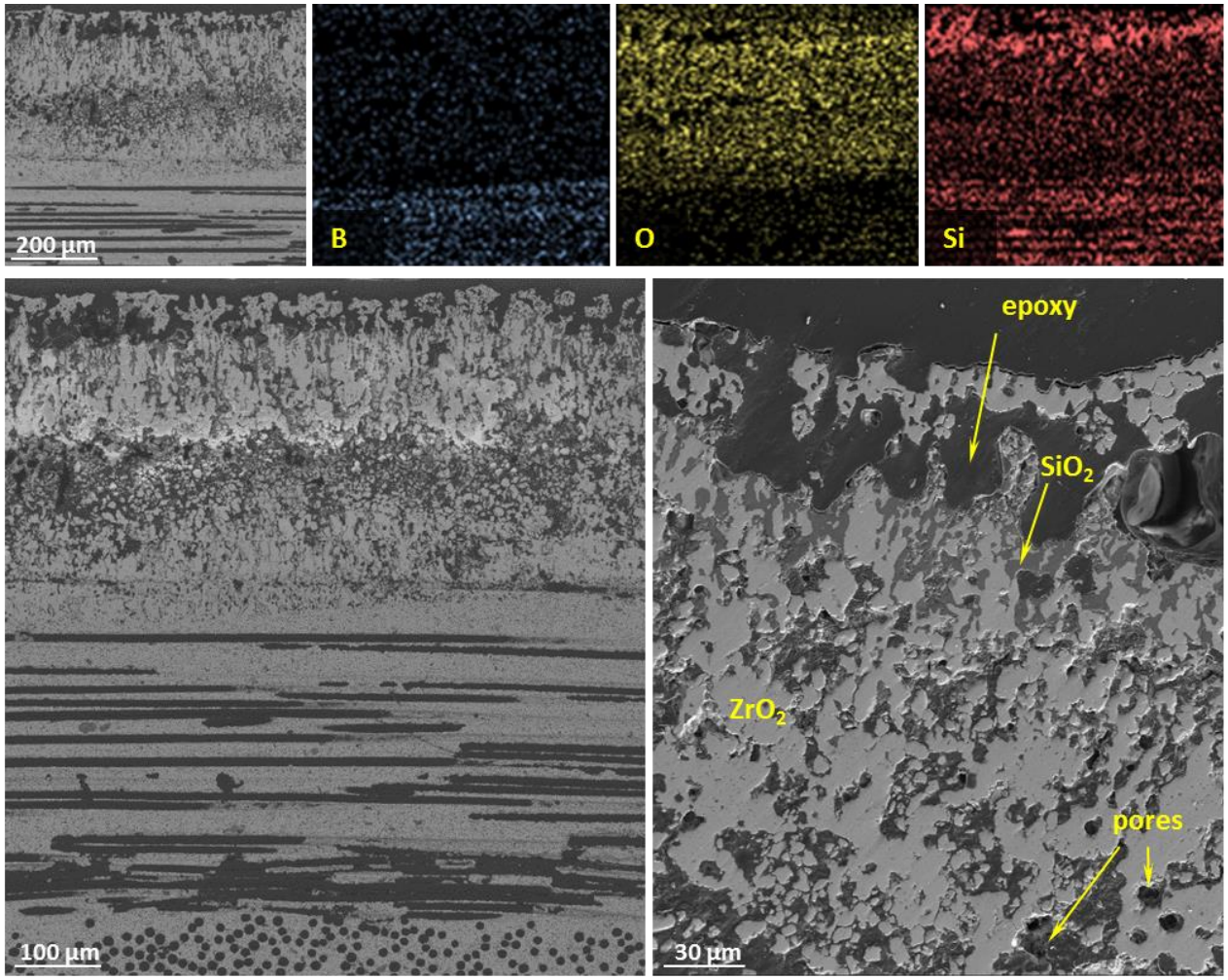

Fig. 17. SEM image of the cross section of the ZS10Y-LF sample after the arc-jet test with corresponding EDS elemental maps showing boron, oxygen and silicon distribution across the profile. Bottom pictures show the outermost oxide layer at higher magnification.

4. Discussion

Several phenomena were observed during UHTCMC samples exposure to arc-jet supersonic plasma flow. A comprehensive interpretation could be proposed, relating the experimental observations to the phase changes occurred on the samples surfaces due to ultra-high-temperature oxidation.

Since the exposed surface had no protective coating, surficial carbon fibers vaporized at relatively low temperature [39], leaving a rough ZrB_2-SiC surface. In agreement with ZrB_2-SiC oxidation mechanism [40, 41], at temperatures below 1400 K (where the spectral emissivity is minimum, roughly 0.3), the sample surface was covered by a boron-oxide glassy phase, as relevant SiC oxidation had not been triggered yet. Between 1500 and 1600 K, SiC underwent passive oxidation and the formation of a stable borosilicate glass (BSG) provided the highest oxidation protection to the UHTC matrix, Fig. 18(a). The maximum emissivity of around 0.75 was reached at temperatures between 1600 and 1700 K, when consistent B_2O_3 vaporization occurred and the glass was mostly composed of SiO_2. In the 2100-2300 K temperature range, which are the maximum temperatures reached before the occurrence of the temperature jump for all the samples, emissivity was then minimum, around 0.5. This is also the temperature range in which the *waves-of-radiance* phenomenon occurred, right before the temperature jump. Since at those temperatures the BSG layer was supposed to be mainly composed of silica, that has a melting point around 2000 K [42], we speculate that the oxide was completely liquid and therefore, in agreement with the discussion by Monteverde et al. [31], the *waves* phenomenon was associated to the shear-induced transportation of the glass along the specimen side surface. The BSG layer is known to perform a protective action for the ceramic, acting as a barrier preventing further oxygen diffusion and consistent material oxidation at intermediate-high temperatures [43]. A combination of shear transportation and volatilization of the glassy phase left the underneath skeleton unprotected, exposing the ZrO_2 grains directly to the supersonic flow [41]. Meanwhile, the residual liquid phase being generated in the sub-scales was not capable to prevent massive volatilization of the gaseous products of SiC and carbon fibers oxidation (SiO, CO_2, CO), whose vapor pressure led to unsteady protrusion and bursting of liquid bubbles, as observed in a previous test campaign [26], Fig. 18(b,c). This is coherent with the microstructural analysis presented in section 3.2, showing that the outer oxide layer on all the samples consisted of porous zirconia, after massive removal of both carbon fibers and silica glass.

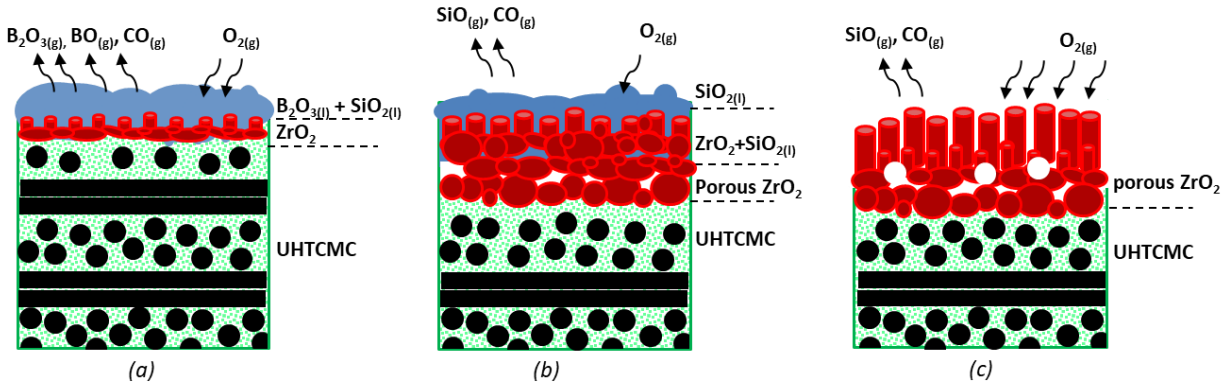

Fig. 18. Sketch of LF UHTCMCs oxidation highlighting three different stages, a) formation of borosilicate glass and compact ZrO_2 layer, b) glass bubbling, development of columnar ZrO_2 outer scale and progressive silica migration outwards from the subscale, c) exposed porous ZrO_2 layer after complete silica shear removal.

At this point, some considerations can be done about the temperature jump, observed for all the samples at a flow total enthalpy over 18 MJ/kg. This phenomenon has been observed by several authors for SiC-containing UHTCs and C-SiC, but a widely agreed interpretation is still lacking. The mechanisms proposed as possible triggers for the jump include transition from passive to active oxidation of silicon carbide [44, 45], triggering of catalytic recombination of nitrogen atoms due to the presence of gaseous silicon [46], formation of cracks promoting oxygen diffusion to inner SiC particles and carbon fibers, resulting in carbon exothermic oxidation and nitridation [44, 47], surface modifications altering properties of the samples such as emissivity and catalycity. All these factors could lead to completely different surface heat flows even under the same test conditions (same arc power, in the present case). It is important to underline that, whatever the reason behind the considerable temperature increase, this was not just a transitory phase, but led to a new condition which persisted for all the remaining test duration. Indeed, the plots of Fig. 4 demonstrate that a steady-state radiative equilibrium temperature was achieved, not only during the maximum enthalpy step, but even during the cooling procedure, in which the torch arc power is stepwise decreased. In the cooling phase, the surface temperature measured by the ISQ5 pyrometer was always higher than during the heating sequence, at all the enthalpy levels. Therefore, after the unsteady evolution corresponding to the trigger of the temperature jump, a new stable equilibrium condition of the heat balance through the exposed surface of the sample must be established, related to variations of the heat flux contributions at the solid/fluid interface.

One possible trigger could be a reduced capability of the material to dissipate the incoming heat flux by radiation. However, in the assumption that, especially at the very high temperatures reached after the jump, the estimated value of spectral emissivity is representative of the total emissivity along the whole wavelength spectrum (as most of the power

is irradiated in the wavelength band around 1 μm, where the value of ε_λ was calculated [48]), it could be argued that the observed increase in the emissivity after the jump should even favor an improved radiative heat dispersion. On the other hand, the general estimated emissivity trend is in agreement with the total emissivity measurements presented by Scatteia et al. [49], while the increase in spectral emissivity with temperature, observed after the occurrence of the jump, is coherent with available data related to total emittance of ZrO_2 at ultra-high-temperature [50], so a different reason is most likely to be searched.

The experimental evidence, with the temperature measurement showing the jump being confined in a thin region in proximity of the sample front surface, and the SEM images revealing a porous oxide layer mainly composed of zirconia, suggests instead that a twofold mechanism could be taken into account to justify the temperature jump:

- a substantial reduction of the thermal conductivity in the oxide layer, on which porosity itself can have a significant influence [51, 52];
- an increased catalytic recombination efficiency due to a transition from an oxide layer mainly covered by glassy silica (relatively low γ_w [53, 54]) to a scale primarily based on zirconia (relatively high γ_w [55]).

In the next section, this interpretation will be quantitatively supported by the outcomes of numerical simulations, which will be compared with the experimental data.

4.1. Numerical simulations

Computational Fluid Dynamic simulations were employed to get more detailed information about the evolution of the aero-thermo-chemical flow field that develops in the facility and around the samples, and to provide possible interpretations for the thermal behavior of the materials.

Specifically, to investigate the phenomenon of the temperature jump, the last step of the test on ZS10Y-LF was selected as a reference case. First, the thermo-fluid-dynamic and chemical field was simulated, employing the numerical models described in section 2.3. Fig. 19 shows the Mach number and temperature distributions inside the mixing chamber and supersonic nozzle of the SPES wind tunnel, in the selected conditions (H_0 = 18 MJ/kg). The hot jet coming from the axial torch is clearly distinguishable.

The conditions obtained at the nozzle exit section were used as inputs for the simulation of the flow field around the test article. Fig. 20(a-d) show the distributions of pressure, temperature and mass fractions of dissociated oxygen and nitrogen. Static pressure and temperature contours evidence the structure of the flow field, with a normal shockwave forming at a distance of 4-5 mm from the sample, and the aforementioned quantities rising downstream the shock to values about 9000 Pa and 6000 K respectively. It is also clear that the level of dissociation of molecular species is considerably high, condition that, as discussed below, results in a relevant effect of surface catalycity on the heat fluxes. Fig. 21 shows in fact the profiles of the cold wall heat flux on the front surface of the sample, for both non-catalytic (NC) and fully catalytic (FC) conditions. It is evident that the heat flux is more than double in the FC condition with respect to the NC, reaching values around 5 MW/m^2.

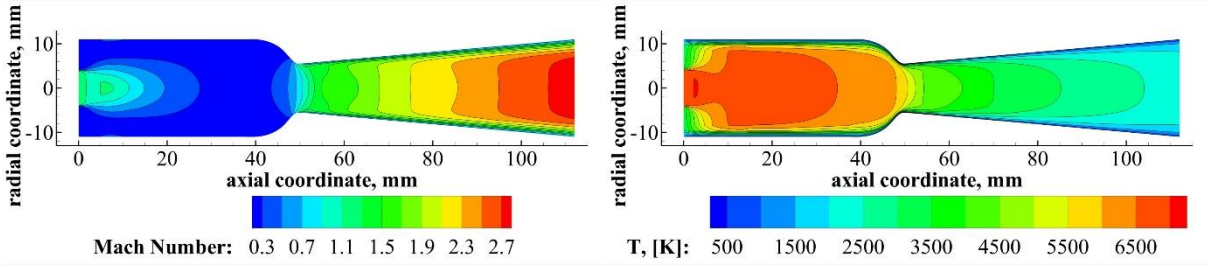

Fig. 19. Distributions of (a) Mach Number and (b) static temperature inside mixing chamber and nozzle, conditions corresponding to Step 7 (H_0 = 18 MJ/kg).

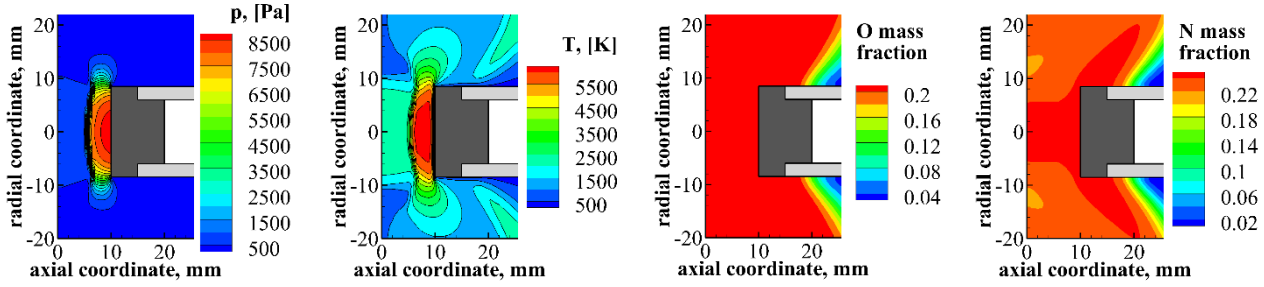

Fig. 20. Distributions of (a) static pressure, (b) static temperature, (c) O mass fraction and (d) N mass fraction around the sample, conditions corresponding to Step 7 (H_0 = 18 MJ/kg).

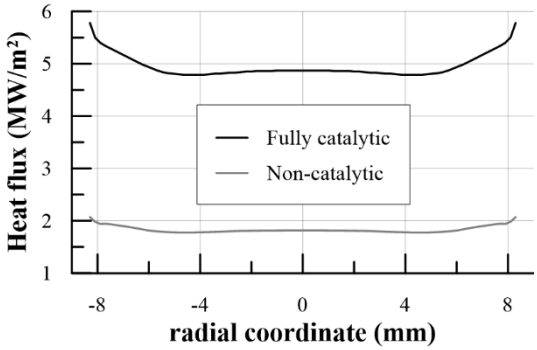

Fig. 21. Non-catalytic and fully catalytic cold wall heat flux profiles on the front surface of the samples, conditions corresponding to Step 7 (H_0 = 18 MJ/kg).

The aero-thermo-chemical field was finally coupled to the thermal analysis of the sample, performing steady-state simulations to match the temperature distribution evaluated by the thermo-camera before and after the temperature jump. The sample density was set to 4300 kg/m^3. The surface emissivity, based on the estimation presented in section 3.1, was set to 0.5 before the jump, and to 0.8 after the jump. In order to match the temperature axial profile before the jump, and based on experimental measurements performed within the frame of the project, a temperature dependent thermal conductivity was considered, varying between 49 W/ m·K at room temperature to 47 W/m·K over 2273 K. Even before the occurrence of the temperature jump, a certain amount of catalytic recombination needed to be taken into account, with a catalytic efficiency $\gamma_w = 4 \cdot 10^{-3}$. This value is representative of SiO_2 [53], which is supposed to be the component with the highest concentration in the BSG phase before the jump. As discussed in section 3.1, at the earliest stages of the temperature jump phenomenon, a liquid phase is transported downstream by the supersonic flow, generating the *waves-of-radiance* phenomenon. It is opinion of the authors that this is the trigger for an unsteady variation of the surface chemistry, resulting in a complete removal of SiO_2 and carbon fibers from the sub-scale layer of the oxide phase, which proceeds until a new radiative equilibrium condition is reached, corresponding to the exposure of a highly porous ZrO_2 scale (see Fig. 17). As anticipated above, to justify the rise in temperature associated to the jump, and localized in the front part of the sample, a double effect was considered: an increase in catalytic activity (γ_w), and a dramatic decrease in thermal conductivity in the oxidized region (k_{ox}). An excellent agreement between numerical and experimental results was obtained assuming $\gamma_w = 7 \cdot 10^{-2}$ (more than one order of magnitude higher than before the jump) and k_{ox} = 1 W/m·K, and considering an oxide thickness of 400 μm (based on the estimations made by the microstructural analyses presented in section 3.2). The comparison between numerical and experimental temperature axial profiles is shown in Fig. 22.

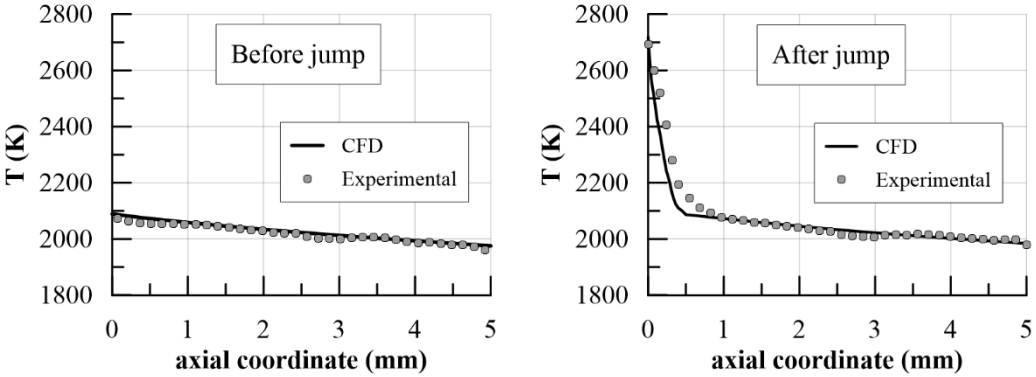

Fig. 22. Comparison between numerical and experimental temperature axial profiles, before (left) and after (right) temperature jump, for sample ZS10Y-LF.

The results of these CFD simulations support the proposed interpretation for the temperature jump, demonstrating that, with reasonable assumptions about the involved physical parameters, it is possible to accurately reproduce the experimental behavior of the UHTCMCs, providing a sufficiently solid explanation of the temperature jump phenomenon.

5. Conclusions

An experimental campaign was carried out to characterize a new class of Ultra-High-Temperature Ceramic Matrix Composites based on ZrB_2-SiC-Y_2O_3 matrix and different carbon fibers architectures, in an environment representative of atmospheric re-entry. Small sized samples were exposed to a supersonic flow of simulated air in an arc-jet wind

tunnel, at specific total enthalpies up to 20 MJ/kg, at heat fluxes over 5 MW/m^2 (cold wall, fully catalytic) and in a highly reactive chemical environment. All samples demonstrated an excellent ablation resistance, with erosion rates on the order of 10^{-4} mm/s. The surface temperature was monitored by non-intrusive infrared equipment, including two-color pyrometers and a thermo-camera. In all the tests, a spontaneous temperature jump of several hundred degrees was observed at constant flow conditions, with maximum equilibrium surface temperatures of 2690-2850 K. Only a thin layer in the front part of the samples, directly exposed to the flow, experienced the jump, while the rear material kept a much lower temperature (below 2200 K even after the jump). A phenomenon of liquid phase transportation along the side of the sample (*waves-of-radiance*) was observed on the samples right before the onset of the jump. The combined effort of experimental activities and numerical simulations allowed proposing a novel and comprehensive interpretation for the jump, based on a twofold mechanism affecting the heat transfer to the material, associated to the formation of a porous ZrO_2 layer on the external surface of the sample after complete removal of the liquid SiO_2 glassy phase: an increase in the catalytic activity and a strong reduction in thermal conductivity in the oxidized region. Despite the jump, the analyzed ceramics displayed promising performance, with an excellent ablation resistance at 2700-2800 K and the capability of the oxide phase to shelter the underneath material, keeping it at acceptable temperatures.

6. Acknowledgements

This study has received funding by the European Union's Horizon2020 research and innovation programme under the research project C^3HARME with Grant Agreement No. 685594.

References

[1] W.G. Fahrenholtz, G.E. Hilmas, Ultra-high temperature ceramics: Materials for extreme environments, Scripta Materialia 129 (2017) 94-99.

[2] E. Wuchina, E. Opila, M. Opeka, W. Fahrenholtz, I. Talmy, UHTCs: Ultra-High Temperature Ceramic materials for extreme environment applications, Electrochem. Soc. Interface 16 (2007) 30-36.

[3] L. Silvestroni, H-J. Kleebe, W.G. Fahrenholtz, J. Watts Super-strong materials for temperatures exceeding 2000°C, Sci. Rep. 7 (2017), 40730, doi: 10.1038/srep40730.

[4] R. Savino, S. Mungiguerra, G.D. Di Martino, Testing ultra-high-temperature ceramics for thermal protection and rocket applications, Adv. Appl. Ceram. 117 (sup1) (2018) s9-s18.

[5] A. Cecere, R. Savino, C. Allouis, F. Monteverde, Heat transfer in ultra-high temperature advanced ceramics under high enthalpy arc-jet conditions, Int. J. Heat Mass Transf. 91 (2015) 747-755.

[6] L. Silvestroni, D. Sciti, Oxidation of ZrB_2 ceramics containing SiC as particles, whiskers, or short fibers, J. Am. Ceram. Soc. 94 (2011) 2796–2799. doi:10.1111/j.1551-2916.2011.04726.x.

[7] A. Purwar, V. Thiruvenkatam, B. Basu, Experimental and computational analysis of thermo-oxidative-structural stability of ZrB_2–SiC–Ti during arc-jet testing, J. Am. Ceram. Soc. 100 (10) (2017) 4860-4873.

[8] P.J. Ritt, P.A. Williams, S.C. Splinter, J.H. Perepezko, Arc jet testing and evaluation of Mo–Si–B coated Mo and SiC–ZrB_2 ceramics, J. Eur. Ceram. Soc. 34 (15) (2014) 3521-3533.

[9] F. Monteverde, D. Alfano, R. Savino, Effects of LaB_6 addition on arc-jet convectively heated SiC-containing ZrB2-based ultra-high temperature ceramics in high enthalpy supersonic airflows, Corros. Sci. 75 (2013) 443-453.

[10] L. Zoli, V. Medri, C. Melandri, D. Sciti, Continuous SiC fibers-ZrB_2 composites, J. Eur. Ceram. Soc. 35 (16) (2015) 4371-4376.

[11] E. P. Simonenko, D.V. Sevast'yanov, N.P. Simonenko, V.G. Sevast'yanov, N.T. Kuznetsov, Promising Ultra-High-Temperature Ceramic Materials for Aerospace Applications, Rus. J. Inorg. Chem. 58 (14) (2013) 1669–1693.

[12] T.A. Parthasarathy, D. Petry, M.K. Cinibulk, T. Mathur, M.R. Mark, R. Gruber, Thermal and Oxidation Response of UHTC Leading Edge Samples Exposed to Simulated Hypersonic Flight Conditions, J. Am. Ceram. Soc. 96 (3) (2013) 907-915.

[13] A.N. Astapov, Yu.S. Pogozhev, M.V. Prokofiev, A.Yu. Potanin, E.A. Levashov, V.I. Vershinnikov, L.N. Rabinskiy, Kinetics and mechanism of the oxidation of $ZrSi_2$-$MoSi_2$-ZrB_2 ceramics in air at temperatures up to 1400 °C, Int. J. Heat Mass Transf. 140 (2019) 12-20.

[14] S. Tang, C. Hu, Design, Preparation and Properties of Carbon Fiber Reinforced Ultra-High Temperature Ceramic Composites for Aerospace Applications: A Review, J. Mater. Sci. Technol. 33 (2) (2017) 117-130, doi: 10.1016/j.jmst.2016.08.004.

[15] L. Zoli, D. Sciti, Efficacy of a ZrB_2–SiC matrix in protecting C fibres from oxidation in novel UHTCMC materials, Mater. Des. 113 (2017) 207–213. doi:10.1016/j.matdes.2016.09.104.

[16] A. Vinci, L. Zoli, D. Sciti, J. Watts, G. E. Hilmas, W. G. Fahrenholtz, Influence of fibre content on the strength of carbon fibre reinforced HfC/SiC composites up to 2100 °C, J. Eur. Ceram. Soc., 39, 2019, 3594-3603 doi:/10.1016/j.jeurceramsoc.2019.04.049.

[17] A. Vinci, L. Zoli, D. Sciti, J. Watts, G. E. Hilmas, W. G. Fahrenholtz, Mechanical behaviour of carbon fibre reinforced TaC/SiC and ZrC/SiC composites up to 2100°C, J. Eur. Ceram. Soc., 39, 2019, 780-787 doi:10.1016/j.jeurceramsoc.2018.11.017.

[18] L. Zoli, A. Vinci, P. Galizia, C. Melandri, D. Sciti, On the thermal shock resistance and mechanical properties of novel unidirectional UHTCMCs for extreme environments, Sci. Rep. 8 (2018) 9148.

[19] A. Vinci, L. Zoli, D. Sciti, M. Cesare, S. Guicciardi, Understanding the mechanical properties of novel UHTCMCs through random forest and regression tree analysis, Mater. Des. 145 (2018) 97–107. doi:10.1016/j.matdes.2018.02.061.

[20] A. Vinci, L. Zoli, E. Landi, D. Sciti, Oxidation behaviour of a continuous carbon fibre reinforced ZrB_2–SiC composite, Corros. Sci. 123 (2017) 129-138. doi:10.1016/j.corsci.2017.04.012.

[21] P. Galizia, S. Failla, L. Zoli, D. Sciti, Tough salami-inspired C_f/ZrB_2 UHTCMCs produced by electrophoretic deposition, J. Eur. Ceram. Soc. 38 (2018). doi:10.1016/j.jeurceramsoc.2017.09.047.

[22] L. Silvestroni, D. Dalle Fabbriche, C. Melandri, D. Sciti, Relationships between carbon fiber type and interfacial domain in ZrB2-based ceramics, J. Eur. Ceram. Soc. 36 (2016) 17–24. doi:10.1016/j.jeurceramsoc.2015.09.026.

[23] A. Purwar, V. Thiruvenkatam, B. Basu, Experimental and computational analysis of thermo-oxidative-structural stability of ZrB_2–SiC–Ti during arc-jet testing, J. Am. Ceram. Soc. 100 (10) (2017) 4860-4873.

[24] P.J. Ritt, P.A. Williams, S.C. Splinter, J.H. Perepezko, Arc jet testing and evaluation of Mo–Si–B coated Mo and SiC–ZrB2 ceramics, J. Eur. Ceram. Soc. 34 (15) (2014) 3521-3533.

[25] C^3HARME Project Website: https://c3harme.eu/.

[26] S. Mungiguerra, G. D. Di Martino, A. Cecere, R. Savino, L. Silvestroni, L. Zoli, A. Vinci e D. Sciti, Arc-jet wind tunnel characterization of ultra-high-temperature ceramic matrix composites, Corr. Sci. 149 (2019) 18-28.

[27] J. Marschall, D. Pejakovic, W.G. Fahrenholtz, G.E. Hilmas, F. Panerai, O. Chazot. Temperature Jump Phenomenon During Plasmatron Testing of ZrB_2-SiC Ultrahigh-Temperature Ceramics, J. Thermoph. Heat Transf. 26 (4) (2012) 559-572.

[28] L. Silvestroni, S. Mungiguerra, D. Sciti, G.D. Di Martino, R. Savino, Effect of hypersonic flow chemical composition on the oxidation behavior of a super-strong UHTC, Corros. Sci. 159 (2019) 108125.

[29] L. Silvestroni, C. Melandri, V. Venkatachalam, J. Binner, D. Sciti, Merging toughness and oxidation resistance in a light ZrB_2 composite, Mater. Des., 183 (2019) 108078.

[30] D. Sciti, L. Zoli, L. Silvestroni, A. Cecere, G.D. Di Martino, R. Savino, Design, fabrication and high velocity oxy-fuel torch tests of a Cf-ZrB_2-nozzle to evaluate its potential in rocket motors, Mater. Des. 109 (2016) 709–717.

[31] F. Monteverde, A. Cecere, R. Savino, Thermo-chemical surface instabilities of SiC-ZrB_2 ceramics in high enthalpy dissociated supersonic air flows, J. Eur. Ceram. Soc. 37 (6) (2017) 2325-2341.

[32] R. Savino, L. Criscuolo, G.D. Di Martino, S. Mungiguerra, Aero-thermo-chemical characterization of ultra-high-temperature ceramics for aerospace applications, J. Eur. Ceram. Soc. 38 (8) (2018) 2937-2953.

[33] M.G. Dunn, S.W. Kang, Theoretical and Experimental Studies of Re-entry Plasmas, *NASA CR-2252*, 1973

[34] S. Gordon, B.J. McBride, Computer Program of Complex Chemical Equilibrium Compositions and Applications, NASA Reference Publication 1311, 1994.

[35] O.N. Suslov, G.A. Tirskiy, The kinetics of the recombination of nitrogen atoms on high temperature reusable surface insulation in hypersonic thermo-chemical non-equilibrium flow, 2nd European Symposium on Aerothermodynamics for Space Vehicles, Noordwijk, The Netherlands, November 1994 (ESA SP-367, February 1995).

[36] S.M. Scala, Hypersonic Heat Transfer to Catalytic Surfaces, Ramo-Wooldridge Second Symposium on Ballistic Missiles, Los Angeles, California, June 1957.

[37] S. Mungiguerra, G.D. Di Martino, G. Zuppardi, Computational Evaluation of Aero-Thermo-Dynamic Loads and Effect of Catalyticity in an Arc-Jet Wind Tunnel, J. Aerosp. Eng. 33 (3) (2020), doi: 10.1061/(ASCE)AS.1943-5525.0001114.

[38] P. Hu, K. Gui, Y. Yang, S. Dong, X. Zhang, Effect of SiC Content on the Ablation and Oxidation Behavior of ZrB2-Based Ultra High Temperature Ceramic Composites, Mater. 6 (5) (2013) 1730–1744.

[39] A. Vinci, L. Zoli, D. Sciti, Influence of SiC content on the oxidation of carbon fibre reinforced ZrB_2/SiC composites at 1500 and 1650 °C in air, J. Eur. Ceram. Soc. 38 (11) (2018) 3767-3776.

[40] P. Hu, W. Guolin e Z. Wang, Oxidation mechanism and ressistance of ZrB_2-SiC composites, Corr. Sci., 51 (2009) 2724-2732.

[41] T. A. Parthasarathy, R.A. Rapp, M. Opeka, M.K. Cinibulk, Modeling Oxidation Kinetics of SiC-Containing Refractory Diborides, J. Amer. Ceram. Soc., 95 (1) (2012) 338-349.

[42] W.M. Haynes, CRC Handbook of Chemistry and Physics, 92nd ed., Boca Raton, FL: CRC Press, 2011.

[43] S. Gangireddy, S. Nanna Karlsdottir, J.W. Halloran, Liquid Oxide Flow During Oxidation of Zirconium Diboride-Silicon Carbide Ultra High Temperature Ceramics, Key Eng. Mater. 434-435 (2010) 144-148, doi: 10.4028/www.scientific.net/KEM.434-435.144

[44] I. Sakraker, C.O. Asma, Experimental investigation of passive/active oxidation behavior of SiC based ceramic thermal protection materials exposed to high enthalpy plasma, J. Eur. Ceram. Soc. 33 (2013) 351-359.

[45] M. Balat-Pichelin, L. Charpentier, F. Panerai, O. Chazot, B. Helber, K. G. Nickel, Passive/active oxidation transition for CMC structural materials designed for the IXV vehicle reentry phase, J. Eur. Ceram. Soc. 35 (2) (2015) 487-502.

[46] H. Hald, Operational limits for reusable space transportation systems due to physical boundaries of C/SiC materials, Aerosp. Sci. Technol. 7 (7) (2003) 551-559.

[47] G. Herdrich, M. Fertig, S. Löhle, S. Pidan, M. Auweter-Kurtz, T. Laux, Oxidation behavior of Silicon carbide-based materials by using new probe techniques, J. Spacecr. Rocket 42 (5) (2015) 817-824.

[48] R. Siegel, J.R. Howell, Thermal radiation heat transfer, Taylor & Francis, Inc., New York, 1978.

[49] L. Scatteia, D. Alfano, F. Monteverde, J.-L. Sans, M. Balat-Pichelin, Effect of the Machining Method on the Catalycity and Emissivity of ZrB_2 and ZrB_2–HfB_2-Based Ceramic, J. Am. Ceram. Soc. 91(5) (2008) 1461–1468.

[50] V.A. Petrov, A.Y. Vorobyev, A.P. Chernyshev, Thermal radiation and optical properties of cubic zirconia stabilised with yttria up to the temperature of high rate evaporation, High Temp. High Press. 34 (2002) 657-668.

[51] K.W. Schlichting, N.P. Padture, P.G. Klemens, Thermal conductivity of dense and porous yttria-stabilized zirconia, J. Mater. Sci. 36 (2001) 3003-3010.

[52] B. Nait-Ali, K. Haberko, H. Vesteghem, J. Absi, D.S. Smith, Thermal conductivity of highly porous zirconia, J. Eur. Ceram. Soc. 26 (2006) 3567–3574.

[53] L. Bedra, M. Balat-Pichelin, Comparative modeling study and experimental results of atomic oxygen recombination on silica-based surfaces at high-temperature, Aerosp. Sci. Technol. 9 (2005) 318–328.

[54] Y. Yang, I. Kim, G. Park, Experimental and numerical study of oxygen catalytic recombination of SiC-coated material, Int. J. Heat Mass Transf. 143 (2019) 118510.

[55] M. Balat-Pichelin, M. Passarelli, A. Vesel, Recombination of atomic oxygen on sintered zirconia at high temperature in non-equilibrium air plasma, Mater. Chem. Phys. 123 (2010) 40–46.